Magnetic-Field Generation by Rayleigh–Taylor Instability in Laser-Driven Planar Plastic Targets

Target designs predicted to achieve ignition by inertial confinement fusion (ICF) rely on understanding Rayleigh–Taylor (RT) instability.[1–3] When an ICF capsule is imploded, the ablation front during the acceleration phase and the pusher–fuel interface during the deceleration and stagnation phases are RT unstable.[4,5] At the unstable interface, spikes of higher-density plasma penetrate into lower-density plasma and bubbles of lower-density plasma rise through the higher-density plasma. Understanding RT instability is important because it can amplify capsule perturbations and destroy implosion uniformity.

Previous theoretical work showed that a plasma subject to RT instability should generate spontaneous magnetic fields.[6,7] These fields may exist in inertial fusion plasmas and modify electron thermal transport.[8,9] If present and unaccounted for, these fields may degrade implosion performance compared to theoretical predictions.[10–12] Magnetic fields can be generated in high-energy-density plasmas by many different mechanisms,[13] including the thermoelectric effect,[14,15] anisotropic hot-electron velocity distributions,[16] and thermoelectric instability.[17] Recently the first measurement of RT-induced magnetic fields was reported,[18] which showed RT-induced magnetic fields in laser-accelerated targets with preimposed target-surface modulations from experiments on the OMEGA Laser System.[19] Magnetic fields with strengths of up to 0.1 MG were inferred in the linear growth phase of RT instability using face-on monoenergetic proton radiography.[20] The monoenergetic protons were generated from D–^{3}He fusion inside an imploding capsule.

This article reports on magnetic-field generation during the nonlinear growth phase of RT instability in an ablatively driven plasma using ultrafast laser-driven proton radiography.[21] Thin plastic foils were irradiated with ~4-kJ, 2.5-ns laser pulses focused to ~10^{14} W/cm^2 on LLE's OMEGA EP Laser System.[22] The driven foils were probed with an ultrafast proton beam that revealed the magnetohydrodynamic (MHD) evolution of the target. The target modulations were seeded by laser nonuniformities and amplified during the target-acceleration phase. These experiments show, for the first time, MG-level magnetic fields inside a laser-driven foil broken apart by RT instability. The experimental results are consistent with two-dimensional (2-D) MHD calculations using the code *DRACO*.[23,24]

Figure 131.18 shows a schematic of the experimental setup. Two long-pulse beams irradiated a 15- or 25-μm-thick CH foil.
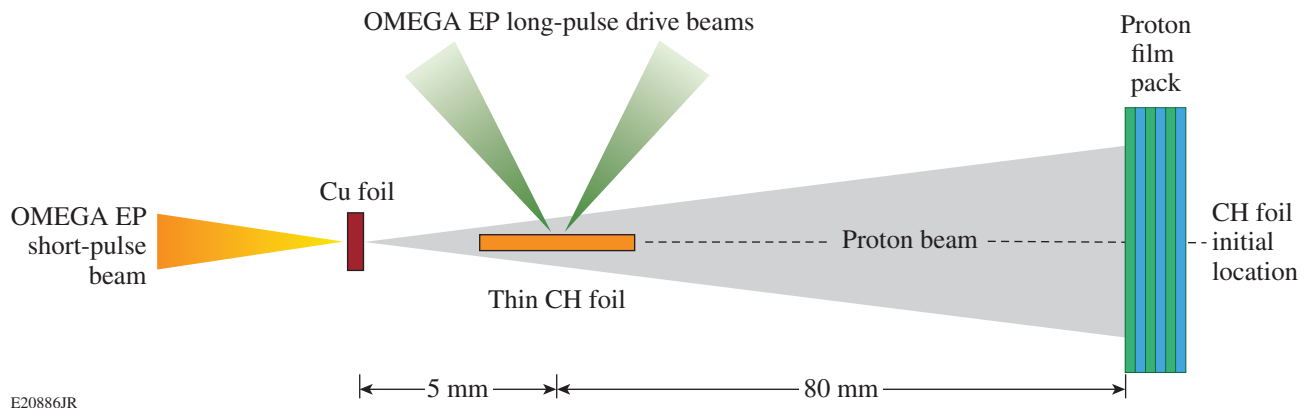
E20886JR

Figure 131.18
Experimental setup.

The foil area was 5×5 mm^2. Only a central ~1-mm-diam part of the foil was driven. Each laser beam delivered an ~2-kJ pulse with a wavelength of 351 nm and a 2.5-ns square temporal profile at 23° to the target normal. The laser beams were focused to ~850-μm-diam focal spots using distributed phase plates.[25] The average overlapped intensity was ~4×10^{14} W/cm^2.

The CH foil was probed in a direction orthogonal to the main interaction with an ultrafast proton beam.[26,27] The proton source was generated by irradiating a planar, 20-μm-thick Cu foil with an ~1-kJ, 10-ps pulse at a wavelength of 1.053 μm. The laser pulse was focused with a 1-m-focal-length, $f/2$ off-axis parabolic mirror onto the Cu foil at normal incidence, providing an intensity of ~5×10^{18} W/cm^2. The relative timing between the long-pulse and short-pulse beams was measured with an x-ray streak camera. Protons were accelerated from the surface of the Cu foil to tens of MeV by target normal sheath acceleration (TNSA).[28] The TNSA mechanism generated a highly laminar proton beam with a micron-scale virtual source size,[29] providing high spatial resolution for probing the main interaction with point-projection radiography.[21]

Combining a filtered stack detector with time-of-flight dispersion provided a multiframe imaging capability.[30] The high-energy protons that passed through the driven CH target were detected with a stack of radiochromic film interleaved with aluminum filters. Soft x rays were filtered with an additional aluminum foil on the front surface of the stack. Each film layer recorded a different probe time because the transit time for protons to the CH foil varied with energy. Protons with different energies deposited energy inside various film layers corresponding to their energy-dependent Bragg peak. The temporal coverage obtained in these experiments on a single shot was ~120 ps, with spatial and temporal resolutions of ~5 to 10 μm and ~10 ps, respectively. The image magnification $M = (L + l)/l$, where l is the distance from the proton-source foil to the CH target and L is the distance from the CH target to the radiochromic film detector. For these experiments, M was ~17 to 20, depending on the radiochromic film layer.

Figure 131.19 shows a typical proton radiograph of a 25-μm-thick CH foil unbroken by instability formation. This radiograph was obtained with 13-MeV protons at time $t = t_0 + 2.56$ ns, where t_0 is the arrival time of the long-pulse beams at the target surface. The undriven foil horizon is indicated. The long-pulse beams irradiated the target from the left and the blowoff plasma accelerated the central part of the foil toward the right. The driven foil had a transverse size comparable with the laser focal spot. At this time, the foil had a velocity
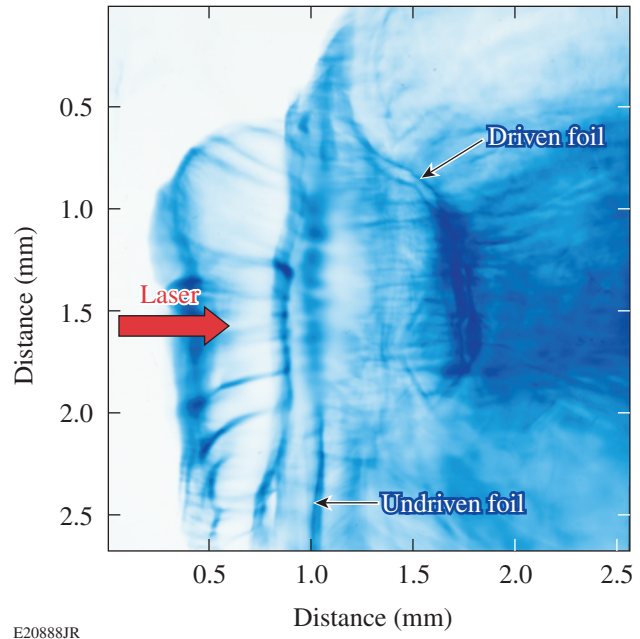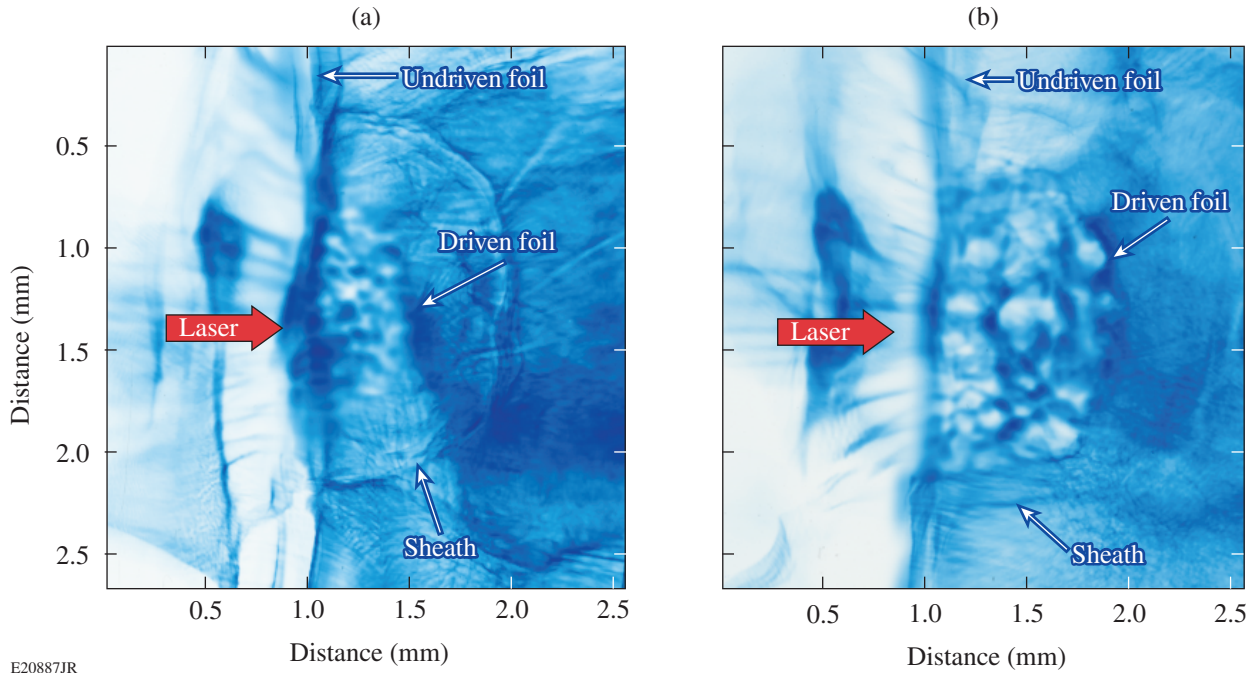

Figure 131.19
Proton radiograph of a 25-μm-thick CH foil taken with 13-MeV protons at $t = t_0 + 2.56$ ns. The laser drive, the undriven foil horizon, and the bow-shaped driven foil are indicated.

of $(3\pm1) \times 10^7$ cm/s, calculated from the measured driven-foil trajectory history.

Thinner-foil targets were broken by instability formation during the acceleration phase. Figure 131.20 shows proton radiographs for a 15-μm-thick CH foil driven with the same laser conditions as the 25-μm-thick foil case. These data were obtained with 13-MeV protons. The relative timing with respect to t_0 was varied from 2.11 ns to 2.56 ns. At $t = t_0 + 2.56$ ns, the foil has traveled a greater distance than the 25-μm-thick foil because less mass was accelerated. In this case, bubble-like structures are observed in the proton radiographs. These perturbations grow in time and show that the target has broken apart during the acceleration phase. Larger-scale structures at $t = t_0 + 2.56$ ns indicate this growth.

Further evidence for the broken foil is provided by the appearance of plasma beyond the driven target. Figure 131.20 shows a plasma sheath ahead of the RT-unstable region. Hot plasma in the laser-ablation region has fed through the compromised foil and formed a halo around the unstable expanding matter. A sheath electric field forms at the plasma/vacuum interface and is detected in the proton radiographs. This effect is not observed in the radiographs of the stable, 25-μm-thick foil, uncompromised by instability growth (see Fig. 131.19).

(a)   (b)

E20887JR

Figure 131.20
Proton radiographs of a 15-μm-thick CH foil taken with 13-MeV protons at (a) $t = t_0 + 2.11$ ns and (b) $t = t_0 + 2.56$ ns. The laser drive, the undriven foil horizon, the RT-unstable plasma, and the sheath field formed by hot-plasma feedthrough are indicated.

The main observation from these data is the electromagnetic fields that are generated during the RT-instability growth. In proton radiography, proton beam density modulations are caused by deflections from electromagnetic fields and by collisional scattering and stopping inside the probed target. For these experiments, collisional scattering and proton stopping are small. For example, collisional energy losses for 13-MeV protons passing through ~30-μm-thick solid CH are $\Delta E/E <$ 1%. Electromagnetic fields must play a dominant role in generating the bubble-like structures observed in the radiography data. The broken foil is revealed in the data by electromagnetic fields that are generated at the RT-unstable interface.

This interpretation is supported by numerical modeling with the 2-D resistive MHD code *DRACO*.[23,24] *DRACO* has a 2-D cylindrical geometry. The equation governing the magnetic field is

$$\frac{\partial \vec{B}}{\partial t} = \nabla \times (\vec{V} \times \vec{B})$$
$$+ \frac{c}{e}\left[\nabla \times \left(\frac{\nabla p_e}{n_e}\right) - \nabla \frac{(\nabla \times \vec{B}) \times \vec{B}}{4\pi n_e} - \nabla \times \frac{\vec{R_T} + \vec{R_u}}{n_e}\right], \quad (1)$$

where $\vec{B}$ is the magnetic induction, p_e is the electron pressure, n_e is the electron number density, e is the fundamental unit of charge, $\vec{V}$ is the flow velocity, and $\vec{R_T}$ and $\vec{R_u}$ are the thermal and frictional forces,[8] respectively. The second term on the right-hand side of Eq. (1) is the thermoelectric source term that is driven by nonparallel density and temperature gradients. The nonuniform ∇p_e force induces poloidal current loops that wrap around the magnetic toroids. The full Braginskii transport coefficients,[8] including the Nernst term[31] and cross-gradient thermal fluxes, were used to calculate $\vec{R_T}$ and $\vec{R_u}$. The temporal evolution of the laser power was provided by experimental measurements. The seeds for the growth of RT instability in the calculations were pre-imposed surface perturbations with a 50-μm wavelength and a 1-μm peak-to-valley amplitude.

The *DRACO* calculations show a 15-μm-thick foil broken apart by RT instability, generating MG-level magnetic fields at the RT-unstable interface. Figure 131.21(a) shows the calculated target-density profile at $t = t_0 + 2.1$ ns. Density perturbations that have grown by RT instability are greater in extent than the target thickness, breaking the foil apart. Large density and temperature gradients form in this unstable plasma and spontaneously generate MG-level magnetic fields. Figure 131.21(b) shows the predicted magnetic-field distribution at $t = t_0 + 2.1$ ns.

(a) Density (g/cm^3)

(b) Magnetic induction
(toroidal component) (Gauss)
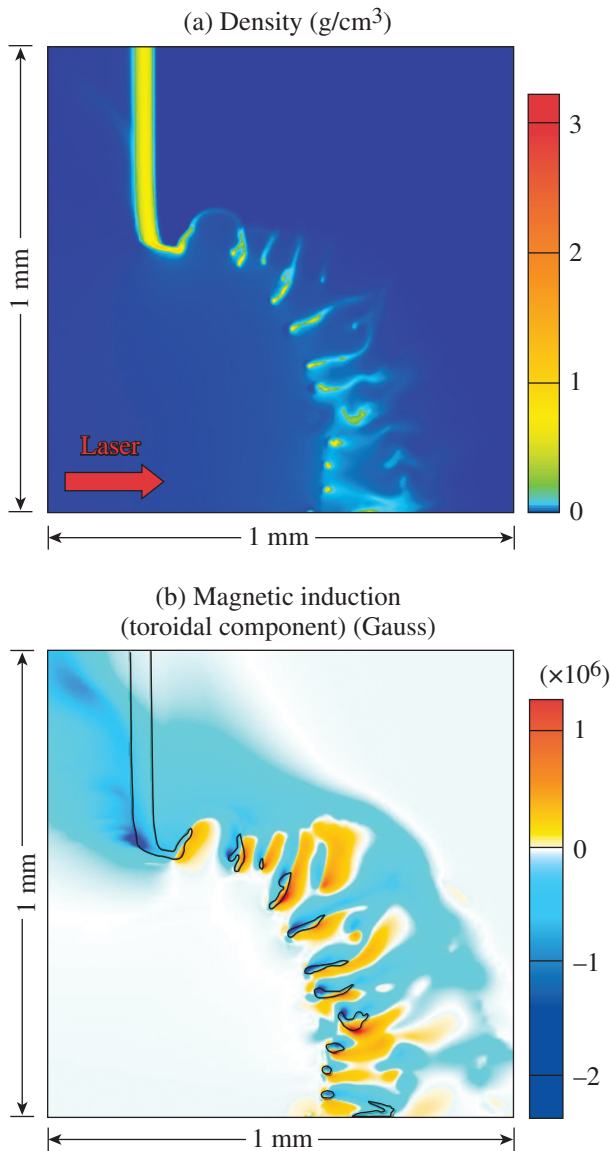
E20889JR

Figure 131.21

(a) Simulated density profile at $t = t_0 + 2.1$ ns. The modeled target is axisymmetric about the horizontal axis. (b) Self-generated magnetic-field distribution at $t = t_0 + 2.1$ ns. The density contour for $\rho = 0.05$ g/cm^3 is overlaid.

Overlaid on this field distribution is the calculated density contour for $\rho = 0.05$ g/cm^3, indicating the position of the target. Magnetic fields generated at the ablation surface are convected toward the lower-density corona by the ablated plasma and to higher-density regions by hot electrons that carry the heat flux (the Nernst effect).[31] In our case, the Nernst convection significantly overperforms the convection by the ablation flow.

Magnetic fields of up to 2 MG are observed in these conditions beyond the coronal plasma and inside the driven foil.

DRACO simulations show that the dynamic effect of the generated magnetic fields on the RT instability is negligible in the linear and the moderately nonlinear stages of its evolution. The fields begin to enhance the RT growth in the highly non-linear stages when the spike sizes are comparable to and larger than the perturbation wavelengths. The *DRACO* calculations reproduce the measured foil velocity to within experimental error, indicating that the gross hydrodynamics of the driven foil are as predicted. For a 25-μm-thick target, *DRACO* calculations show that the RT instability does not break the foil apart and no significant small-scale magnetic fields are generated.

The magnitude of the generated magnetic fields is estimated by measuring the angular deflection θ of protons from their original trajectory while passing through the field region. When the apparent displacement of protons is δ in the target plane, the angular deflection θ is calculated by $\tan\theta = M\delta/D$, where M is the geometric magnification and D is the distance between the main target and the radiochromic film detector. The proton-path–integrated B field caused by the Lorentz force acting upon the proton probe beam is $\int \vec{B} \times d\vec{l} = m_{\mathrm{p}} v \sin\theta/e$, where m_{p} is the proton mass and v is the proton speed. In our experiments, the protons are deflected by azimuthal magnetic fields generated around the RT spikes. At $t = t_0 + 2.11$ ns, a δ of 25 μm results in a deflection angle θ of 0.31°. Assuming an integration path length slightly larger than the target thickness ($L \sim 25$ μm) gives a magnetic-field strength of ~1.4 MG, which is in good agreement with the *DRACO* simulations.

At the RT-unstable interface, narrow spikes are formed where the dense matter falls through the light matter, and bubbles are generated when the light material rises into the dense material.[3] This process generates magnetic fields that wrap around the troughs of the spikes. The growth of the spatial scale length of the perturbed features is caused by magnetic-field evolution as the RT instability develops. The magnetic-field topology in *DRACO* is different from the real three-dimensional (3-D) situation. In 3-D RT instability, azimuthal magnetic fields are formed around single spikes and bubbles. The magnitude and the predominant wavelength of the magnetic fields, however, are expected to be accurate.

A proton ray-tracing code using electromagnetic field distributions from the 2-D *DRACO* calculations supports

the dominant role of magnetic fields in deflecting protons in these experiments. The initial proton-source details and the radiography geometry were taken from the experiments. The accumulated proton numbers were monitored in the ray-tracing code at a simulated detector plane. Figure 131.22 shows the effect of electric and magnetic fields in this process. The predicted proton distribution is unchanged when electric fields are turned off in the calculations, while few proton deflections are observed when magnetic fields are turned off. Self-generated magnetic fields at the RT-unstable interface are the dominant cause for proton-beam deflections in these experiments. Two-dimensional Fourier analysis of the measured proton radiographs shows that the characteristic spatial scale length of the bubble-like features at $t = t_0 + 2.11$ ns is ~82 μm, growing to ~115 to 230 μm at $t = t_0 + 2.56$ ns. Broadly consistent with this experimental trend, Fourier analysis of the proton distribution in Fig. 131.22 gives a characteristic spatial scale length of ~93 μm, growing to ~220 μm at the latest time.
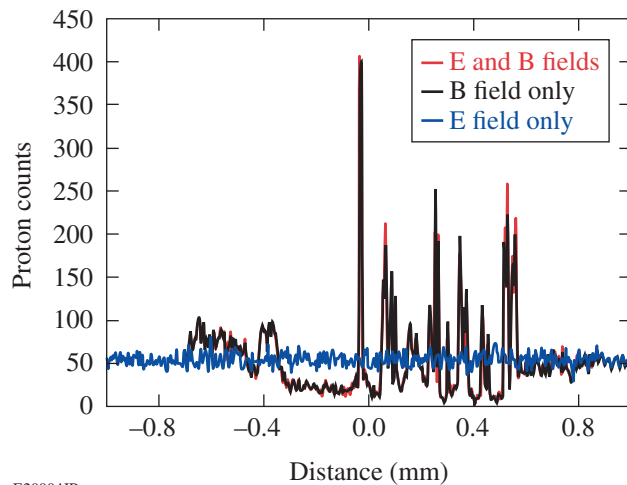
E20904JR

Figure 131.22
Proton tracking code results. Proton deflections are modeled based on electromagnetic-field distributions predicted by 2-D *DRACO* calculations.

In summary, magnetic-field generation during the nonlinear growth of target perturbations by RT instability in ablatively driven foils was studied. Measurements of MG-level magnetic fields were supported by recovering characteristic spatial scale lengths of the proton deflections using a particle ray-tracing code that incorporates electromagnetic-field distributions from a 2-D MHD model. Electric fields were found to be negligible compared to the generated magnetic fields in producing the modulated patterns in the proton radiography beam profile. Simulations suggest that the dynamic effect of these magnetic fields on RT growth is not significant.

ACKNOWLEDGMENT

REFERENCES

1. Lord Rayleigh, Proc. London Math Soc. **XIV**, 170 (1883).

2. G. Taylor, Proc. R. Soc. London Ser. A **201**, 192 (1950).

3. R. Betti and J. Sanz, Phys. Rev. Lett. **97**, 205002 (2006).

4. J. D. Lindl, Phys. Plasmas **2**, 3933 (1995).

5. R. L. McCrory, D. D. Meyerhofer, S. J. Loucks, S. Skupsky, R. Betti, T. R. Boehly, T. J. B. Collins, R. S. Craxton, J. A. Delettrez, D. H. Edgell, R. Epstein, K. A. Fletcher, C. Freeman, J. A. Frenje, V. Yu. Glebov, V. N. Goncharov, D. R. Harding, I. V. Igumenshchev, R. L. Keck, J. D. Kilkenny, J. P. Knauer, C. K. Li, J. Marciante, J. A. Marozas, F. J. Marshall, A. V. Maximov, P. W. McKenty, S. F. B. Morse, J. Myatt, S. Padalino, R. D. Petrasso, P. B. Radha, S. P. Regan, T. C. Sangster, F. H. Séguin, W. Seka, V. A. Smalyuk, J. M. Soures, C. Stoeckl, B. Yaakobi, and J. D. Zuegel, J. Phys. IV France **133**, 59 (2006).

6. J. A. Stamper *et al.*, Phys. Rev. Lett. **26**, 1012 (1971).

7. K. Mima, T. Tajima, and J. N. Leboeuf, Phys. Rev. Lett. **41**, 1715 (1978).

8. S. I. Braginskii, in *Reviews of Plasma Physics*, edited by Acad. M. A. Leontovich (Consultants Bureau, New York, 1965), Vol. 1, p. 205.

9. M. G. Haines, Phys. Rev. Lett. **78**, 254 (1997).

10. J. A. Stamper, Laser Part. Beams **9**, 841 (1991).

11. R. G. Evans, Plasma Phys. Control. Fusion **28**, 1021 (1986).

12. B. Srinivasan, G. Dimonte, and X.-Z. Tang, Phys. Rev. Lett. **108**, 165002 (2012).

13. M. G. Haines, Can. J. Phys. **64**, 912 (1986).

14. J. A. Stamper and B. H. Ripin, Phys. Rev. Lett. **34**, 138 (1975).

15. D. G. Colombant and N. K. Winsor, Phys. Rev. Lett. **38**, 697 (1977).

16. K. Estabrook, Phys. Rev. Lett. **41**, 1808 (1978).

17. M. G. Haines, Phys. Rev. Lett. **47**, 917 (1981).

18. M. J. E. Manuel, C. K. Li, F. H. Séguin, J. Frenje, D. T. Casey, R. D. Petrasso, S. X. Hu, R. Betti, J. D. Hager, D. D. Meyerhofer, and V. A. Smalyuk, Phys. Rev. Lett. **108**, 255006 (2012).

19. T. R. Boehly, D. L. Brown, R. S. Craxton, R. L. Keck, J. P. Knauer, J. H. Kelly, T. J. Kessler, S. A. Kumpan, S. J. Loucks, S. A. Letzring, F. J. Marshall, R. L. McCrory, S. F. B. Morse, W. Seka, J. M. Soures, and C. P. Verdon, Opt. Commun. **133**, 495 (1997).

20. C. K. Li, F. H. Séguin, J. A. Frenje, J. R. Rygg, R. D. Petrasso, R. P. J. Town, P. A. Amendt, S. P. Hatchett, O. L. Landen, A. J. Mackinnon, P. K. Patel, V. A. Smalyuk, T. C. Sangster, and J. P. Knauer, Phys. Rev. Lett. **97**, 135003 (2006).

21. M. Borghesi *et al*., Phys. Rev. Lett. **92**, 055003 (2004).

22. L. J. Waxer, D. N. Maywar, J. H. Kelly, T. J. Kessler, B. E. Kruschwitz, S. J. Loucks, R. L. McCrory, D. D. Meyerhofer, S. F. B. Morse, C. Stoeckl, and J. D. Zuegel, Opt. Photonics News **16**, 30 (2005).

23. D. Keller, T. J. B. Collins, J. A. Delettrez, P. W. McKenty, P. B. Radha, B. Whitney, and G. A. Moses, Bull. Am. Phys. Soc. **44**, 37 (1999).

24. I. V. Igumenshchev, F. J. Marshall, J. A. Marozas, V. A. Smalyuk, R. Epstein, V. N. Goncharov, T. J. B. Collins, T. C. Sangster, and S. Skupsky, Phys. Plasmas **16**, 082701 (2009).

25. *LLE Review Quarterly Report* **33**, 1, Laboratory for Laser Energetics, University of Rochester, Rochester, NY, LLE Document No. DOE/DP/40200-65, NTIS Order No. DE88008065 (1987).

26. E. L. Clark *et al*., Phys. Rev. Lett. **85**, 1654 (2000).

27. R. A. Snavely, M. H. Key, S. P. Hatchett, T. E. Cowan, M. Roth, T. W. Phillips, M. A. Stoyer, E. A. Henry, T. C. Sangster, M. S. Singh, S. C. Wilks, A. MacKinnon, A. Offenberger, D. M. Pennington, K. Yasuike, A. B. Langdon, B. F. Lasinski, J. Johnson, M. D. Perry, and E. M. Campbell, Phys. Rev. Lett. **85**, 2945 (2000).

28. S. C. Wilks, A. B. Langdon, T. E. Cowan, M. Roth, M. Singh, S. Hatchett, M. H. Key, D. Pennington, A. MacKinnon, and R. A. Snavely, Phys. Plasmas **8**, 542 (2001).

29. T. E. Cowan *et al*., Phys. Rev. Lett. **92**, 204801 (2004).

30. A. J. Mackinnon, P. K. Patel, M. Borghesi, R. C. Clarke, R. R. Freeman, H. Habara, S. P. Hatchett, D. Hey, D. G. Hicks, S. Kar, M. H. Key, J. A. King, K. Lancaster, D. Neely, A. Nikkro, P. A. Norreys, M. M. Notley, T. W. Phillips, L. Romagnani, R. A. Snavely, R. B. Stephens, and R. P. J. Town, Phys. Rev. Lett. **97**, 045001 (2006).

31. A. Nishiguchi, T. Yabe, and M. G. Haines, Phys. Fluids **28**, 3683 (1985).